Downconversion of terahertz radiation due to intrinsic hydrodynamic nonlinearity of a two-dimensional electron plasma

Valeria Giliberti,[1,2] Alessandra Di Gaspare,[1] Ennio Giovine,[1] Michele Ortolani,[1,2] Lucia Sorba,[3] Giorgio Biasiol,[4]
Vyacheslav V. Popov,[5,6] Denis V. Fateev,[5] and Florestano Evangelisti[7]

[1]*CNR-Istituto di Fotonica e Nanotecnologie, Rome 00146, Italy*
[2]*Dipartimento di Fisica, Sapienza Università di Roma, Rome 00185, Italy*
[3]*NEST, CNR-Istituto Nanoscienze and Scuola Normale Superiore, Pisa 56127, Italy*
[4]*Laboratorio TASC, CNR-IOM, Area Science Park, Trieste 34149, Italy*
[5]*Kotelnikov Institute of Radio Engineering and Electronics (Saratov Branch), Saratov 410019, Russia*
[6]*Saratov Scientific Center of the Russian Academy of Sciences, Saratov 410028, Russia*
[7]*Dipartimento di Scienze, Università Roma Tre, Rome 00156, Italy*

We have measured the electric signal downconverted from a terahertz frequency by an unbiased high mobility two-dimensional electron-gas (2DEG) device. The 2DEG was confined in an asymmetric plasmonic microcavity, and the radiation frequency was continuously tuned in the 0.2–0.4 THz range. The presence of resonant peaks at three frequencies corresponding to three plasma oscillation modes of the ungated 2DEG clearly points to the intrinsic nature of the hydrodynamic nonlinearity responsible for the downconversion as opposed to previously proposed plasmonic cavity configurations where the 2DEG oscillates under the metal gate that also acts as the source of the nonlinearity.

The nonlinear nature of hydrodynamic motion in electron fluids becomes apparent when electron plasma waves at terahertz (THz) frequencies are excited in solid-state electronic devices based on materials hosting quantum-confined two-dimensional electron gases (2DEG), such as semiconductor heterostructures and graphene [1–3]. The plasma waves operate as mixers of the excited THz frequencies and produce upconverted signals useful for radiation generation and downconverted signals that can be electrically measured [4]. This mechanism should become very efficient when resonant plasmons are excited in a cavity as the spatiotemporal modulations of the electron density and velocity would then be stronger. However, a simple symmetric one-directional cavity cannot be used because the inversion symmetry along the electric-field direction needs to be broken to observe the upconverted and downconverted signals as is required for every second-order optical nonlinearity. Up to now, resonant cavities for 2DEG plasmons have been implemented in a few cases, using a metal gate to define the cavity geometry and imposing asymmetric boundary conditions for the oscillating electromagnetic potential either at the opposite ends of the gate electrode [5–8] or by differently biasing multiple gate electrodes [9,10]. The presence of a metal plate at distance d from the 2DEG channel much smaller than the gate length L_g has a profound effect on the plasma-wave dispersion laws as the velocity is reduced by screening effects, and the high-frequency cutoff of devices is reduced correspondingly [11]. It would be very important for future infrared and terahertz devices capable of frequency manipulation to fully exploit the nonlinear potential of 2D plasmon oscillations, beyond the field-effect transistor structure. However, a demonstration of the nonlinear nature of plasmons in a freely oscillating, ungated 2D electron fluid is still lacking.

In the present paper, we have experimentally observed resonant downconversion under THz illumination in a 2DEG plasmonic device made of a two-terminal cavity of length L delimited by two identical side metal contacts but made asymmetric by positioning a short gate wire ($L_g \approx d \ll L$) close to the left side contact (see Fig. 1). Based on the excellent agreement of the spectroscopic data with finite-element-method (FEM) spectral simulations of the hydrodynamic motion, we interpret the resonances as the nonlinear downconversion of the radiation signal by asymmetric cavity plasmons of the ungated electron gas. The very short gated channel section is used as a tunable-strength defect producing the asymmetry in ungated plasmon cavity modes, rather than serving as the nonlinear element leading to downconversion in itself. The electrodynamics of our plasmonic device can be described by solving the Maxwell equations together with the one-directional equations of motion of the 2D electron system of density $n(x,t)$ and velocity $v(x,t)$ under the effect of the longitudinal electric field $E_x(x,t)$. One thus obtains a system composed by the Euler equation and the continuity equation [2,12,13],

$$\frac{dv}{dt} + v\frac{dv}{dx} + \frac{v}{\tau} = \frac{e}{m^*}E_x(x,t),$$
$$\frac{dn}{dt} + \frac{d(nv)}{dx} = 0,$$

(1)

where e and m^* are the electron charge and effective mass and $1/\tau$ is the electron-scattering rate with phonons and impurities. The nonlinearity of hydrodynamic equations implies that, under sinusoidal excitation at a frequency ω, this fluid is able to produce both an upconverted optical signal at frequency 2ω and a zero frequency (dc) signal that can be measured between the side metal contacts of the device. It can be demonstrated [2,3] that the amplitude of the nonlinear current (both at 2ω and in dc) is the sum of a term proportional to both linear components of electron-density and velocity modulations plus a "convection term" proportional to the second-order velocity modulations. Since for harmonic
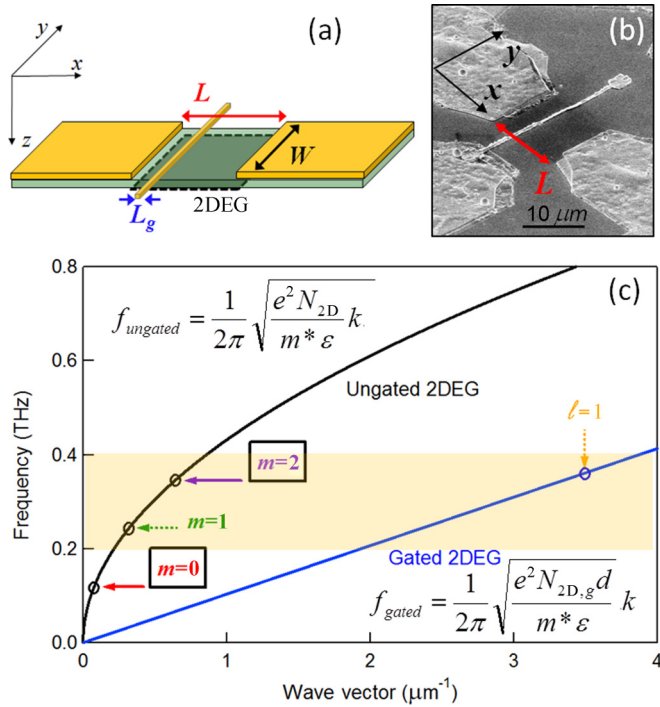
FIG. 1. (Color online) Device concept. Sketch of (a) the core of the device and (b) electron microscope image after fabrication. The plasmon microcavity length $L = 10\,\mu m$ is much longer than the gate length $L_g = 500$ nm and of the gate-to-2DEG distance $d = 200$ nm. The gate finger is shifted from the center by 2.25 μm to provide the nonlinear device with the needed asymmetry. (c) Plasma-wave dispersion relations of the infinite 2DEG sheet confined in a GaAs layer ($\varepsilon = 12.56\varepsilon_0$, $m^* = 0.67m_e$) for the ungated 2DEG ($N_{2D} = 2.2 \times 10^{11}$ cm^{-2}, black curve) and the gated 2DEG ($N_{2D,g} = 0.8 \times 10^{11}$ cm^{-2}, blue curve). The arrows indicate the expected position of the first three cavity resonances of the ungated plasmons (labeled by the index m) and the first resonance of screened plasmons ($l = 1$) when the cavity lengths of our device are used as inputs and the image charge induction in the side metal contacts is considered (see text). The shaded area highlights the frequency range of our experimental setup (0.2–0.4 THz).

excitations the continuity equation requires the above-mentioned terms being proportional to each other, the amplitude of the nonlinear current can also be thought to show a square-law dependence either on the electron-density modulation at ω or on the velocity modulation at ω [2,3].

It is well known [1,14,15] that in order to clearly observe resonant spectroscopic peaks in the dc response due to 2DEG plasmons in a cavity, the excitation has to be practically realized at THz frequencies in high mobility semiconductor heterostructures at low temperature T, where $1/\tau$ is negligible as compared with the electron-electron scattering rate and ω is high enough that $\omega\tau \gg 1$. Moreover, as anticipated, at THz frequencies the plasma wavelength is on the micron scale, and it practically becomes possible to fabricate microcavities for 2D plasma waves by lithography [7,16]. Finally, for submillimeter radiation wavelengths the side metal contacts of the device can be shaped into the two arms of a planar antenna by on-chip metal evaporation [7,17]. Efficient coupling of the 2DEG device to a free-space THz beam can then be obtained

by using a substrate lens (a silicon hyperhemisphere coupled to the on-chip dipole antenna) [7,17–20]. All these experimental facts allowed us to observe the nonlinear electrodynamic response of the ungated 2DEG in the frequency range of 0.2–0.4 THz, but the validity of the physical concepts demonstrated here holds for any 2D electron material, frequency range, and operation temperature where the condition for underdamped oscillatory behavior $\omega\tau \gg 1$ is fulfilled.

In this paper, the 2DEG device is defined as a rectangular portion of a heterostructure wafer containing a 2DEG grown by molecular-beam epitaxy, quantum confined along the growth direction (z coordinate) by conduction-band offset and doping-induced band bending. The heterostructure growth sequence was as follows: semi-insulating GaAs wafer, 500-nm GaAs buffer layer, 500-nm GaAs/Al$_{0.33}$Ga$_{0.67}$As superlattice, 1000-nm i-GaAs layer, 40-nm i-Al$_{0.33}$Ga$_{0.67}$As spacer, δ-doping Si layer, 150-nm i-Al$_{0.33}$Ga$_{0.67}$As layer, and 10-nm i-GaAs cap layer. The undoped Al$_{0.33}$Ga$_{0.67}$As/GaAs heterojunction 40 nm below the δ-doping layer forms the triangular quantum well hosting the 2DEG. The as-grown 2DEG mobility and carrier density parameters measured at $T = 1.5$ K in dark conditions were $\mu = 1.8 \times 10^6$ cm^2 V^{-1} s^{-1} and $N_{2D} = 1.9 \times 10^{11}$ cm^{-2}. In the conditions at which the THz experiment was conducted ($T = 10$ K) we obtained instead $\mu = 3 \times 10^5$ cm^2 V^{-1} s^{-1} and $N_{2D} = 2.2 \times 10^{11}$ cm^{-2}. The 2DEG in the fabricated device was also confined along the y direction by nanolithography (width $W = 10\,\mu m$) and ion implantation and electrically connected to side metal contacts along the x direction [see Figs. 1(a) and 1(b)], which are in turn connected to the planar antenna arms (see Supplemental Material S1 [21]). After device fabrication, the electron density under the gate $N_{2D,g}$ is estimated to be around 0.8×10^{11} cm^{-2} at zero dc gate bias, whereas that of the ungated regions N_{2D} can be generally taken as unchanged during the fabrication process.

We effectively realized an asymmetric charge density at the dipole antenna feed by adding a very short metal gate closer to one of the two side metal contacts defining the device geometry along x as proposed in Ref. [1]. Assuming reflecting behavior for plasma waves at the metal contacts, the entire ungated 2DEG length $L = 10\,\mu m$ forms the resonant cavity. The plasmon modes of this asymmetric cavity can be related to those of a symmetric cavity by using the infinite 2DEG plasmon dispersion relations reported in Fig. 1(c). From here on, we will label the asymmetric cavity plasmons with an index m that counts the number of nodes of the electric-field profile along the x coordinate. The cavity length was chosen such that some of the lowest-frequency resonant plasma modes fall in the 0.2–0.4-THz range of our apparatus. Due to induction of image charges at the side contacts of the device, the resonant wave vector for a cavity of length L is different from $k = \pi(m + 1)/L$. This effect can be quantified by FEM simulations yielding an effective cavity length $L_{\text{eff}}^{(m)} > L$, which is different for each mode and tends to L with increasing mode index [22]. According to FEM simulations, performed with a 2D model with a mesh of variable cell size explicitly accounting for the 2DEG properties, for a 10-μm-long ungated 2DEG cavity the frequency of the first even mode ($m = 0$, $L_{\text{eff}}^{(0)} = 4.50L$) is around 0.10 THz, whereas the second even mode ($m = 2$, $L_{\text{eff}}^{(2)} = 1.96L$) falls in the 0.2–0.4-THz range of our apparatus

(the resonance frequency is 0.346 THz). The introduction of the short gate gives rise to another asymmetric cavity plasmon at 0.250 THz, labeled $m = 1$ with $L_{\text{eff}}^{(1)} = 1.45L$. It corresponds to the inactive first odd mode of the symmetric cavity (in a symmetric cavity this mode has zero net dipole moment).

The short gate of length $L_g = 500$ nm is shifted by 2.25 μm from the center of the cavity [see Figs. 1(a) and 1(b)]. Since $L_g \ll L$, the gate can be considered as a defect in the cavity, and its first-order effect on the plasmon mode dispersion can be neglected [22]. Assuming reflective behavior at the gate ends, a much shorter nanocavity formed by the gate of length $L_g \ll L$ can be considered. For electron density under the gate $N_{2D,g} \sim 0.8 \times 10^{11}$ cm^{-2} and $L_g = 500$ nm, the fundamental resonance of the gated nanocavity, according to the gated plasmon dispersion relation, also falls in the investigated frequency range of 0.2–0.4 THz. This mode is labeled $l = 1$, where l is the modal index for the gated cavity resonant wave vectors $k = \pi l/(L_g + 2d)$ and $d = 200$ nm is the gate-to-channel distance [11]. The much shorter length of the nanocavity thus balances the plasmon slowdown effect due to the screening of the 2DEG by the metal gate electrode [see Fig. 1(c)], making the gated cavity resonance appear in the same frequency range as that of the resonances of the entire ungated cavity. We will see below however that the assumption of reflective behavior at the gate ends is not justified for a short gate so that the gated plasmon mode does not remain isolated from the rest of the device but gives rise to a hybrid (gated-ungated) mode instead [22].

The packaged 2DEG plasmonic device was mounted in a closed-cycle cryostat with optical access and cooled down to $T = 10$ K. The radiation emitted by a voltage-tunable amplifier-multiplier chain (by Virginia Diodes, Inc.) with frequency swept in the 0.2–0.4 THz range was focused onto the substrate lens. The THz source was on-off amplitude modulated by a master oscillator at 1 kHz, and the electric current generated in the device was measured by a lock-in amplifier in the absence of a dc bias applied to the side metal contacts. The nonlinear nature of the measured current signal is clearly demonstrated by the simultaneous detection of the optical power produced by second-harmonic generation in our device. In the inset of Fig. 2(b), we report the dependence on the incident excitation power at $f = 2\pi\omega = 0.165$ THz of both the current signal and the emitted optical power integrated in the 0.22–0.36 THz window. The current signal shows a linear dependence on the incident excitation power as in any nonlinear square-law detector, and the upconverted optical power (which we identify with second-harmonic generation and reemission at 0.330 THz) is quadratic with the excitation power. This control experiment is sketched in Fig. 2(a) and fully described in the Supplemental Material S5 [21].

The measured downconverted signal at $T = 10$ K as a function of frequency is shown in Fig. 2(b) for two different values of $N_{2D,g}$. It displays three main peaks around 0.25, 0.35, and 0.37 THz which fade out with increasing T above 90 K (see Supplemental Material S3 [21]). The intensity of the peak at 0.35 THz is lower with respect to the others. The positions of the peaks at 0.25 and 0.35 THz quite well match the $m = 1$ and $m = 2$ modes as calculated in Fig. 1(c). Intriguingly, the peak at 0.37 THz approximately corresponds to the $l = 1$ mode of the gated 2DEG cavity for $N_{2D,g} = 0.8 \times 10^{11}$ cm^{-2}.
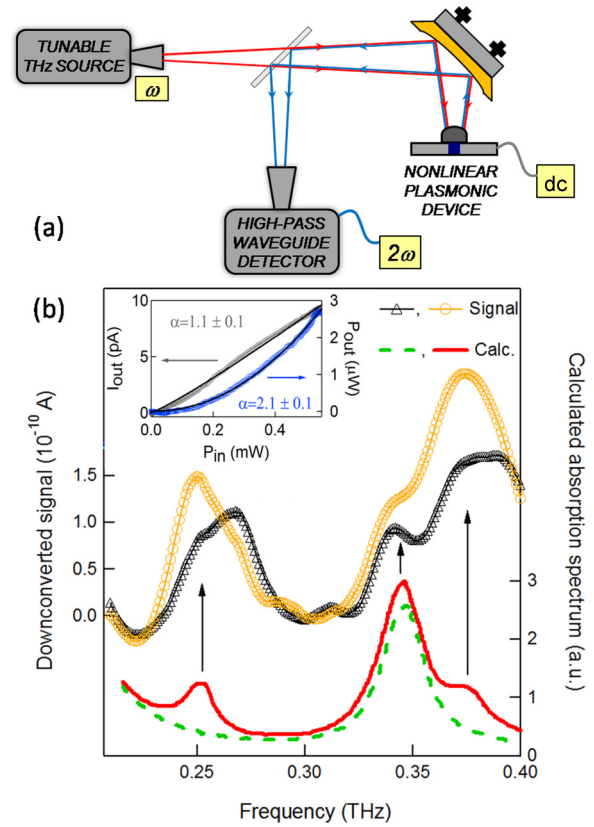

FIG. 2. (Color online) (a) Sketch of the experimental setup used for the second-harmonic generation experiment where the high-pass waveguide detector was used to measure the emitted optical power in the 0.22–0.36-THz window. (b) Comparison of experimental downconversion spectra measured from the device (symbols, left scale) with the calculated absorption spectra (curves, right scale) for a symmetric cavity of length $L = 10\,\mu$m without a gate (dashed green curve) and for our asymmetric device (continuous red curve). The black triangles refer to the spectrum measured with the gated region in accumulation mode ($N_{2D,g} \sim N_{2D} = 2.2 \times 10^{11}$ cm^{-2}), whereas the orange circles refer to $N_{2D,g} \sim 0.8 \times 10^{11}$ cm$^{-2} < N_{2D}$ (stronger cavity defect). The equilibrium electron-density values used in the calculations are $N_{2D} = 2.2 \times 10^{11}$ and $N_{2D,g} = 0.8 \times 10^{11}$ cm^{-2} for the ungated and gated 2DEG regions, respectively. The inset: dependence on the incident power P_{in} at 0.165 THz and power-law fits of the current signal (I_{out}, gray squares) and of the emitted optical power in the 0.22–0.36-THz window (P_{out}, blue circles).

This resonant peak originates from a hybrid plasmon mode triggered by the resonant plasmon of the gated nanocavity in the entire ungated cavity as explained below. The good correspondence between the frequency of experimental peaks and that of expected plasma modes suggests that excitation of resonant plasma waves at specific frequencies results in strong spatiotemporal modulation of the electron density and electron velocity in the 2DEG, which in turn produces the downconverted peaks at the same frequencies due to the intrinsic nonlinearity of the free-electron motion. This is the main result of the present paper, and it is validated by a direct comparison between the experimental spectrum and the absorption spectrum computed by FEM simulations of the *symmetric* cavity (with no gate at all) and with that of the
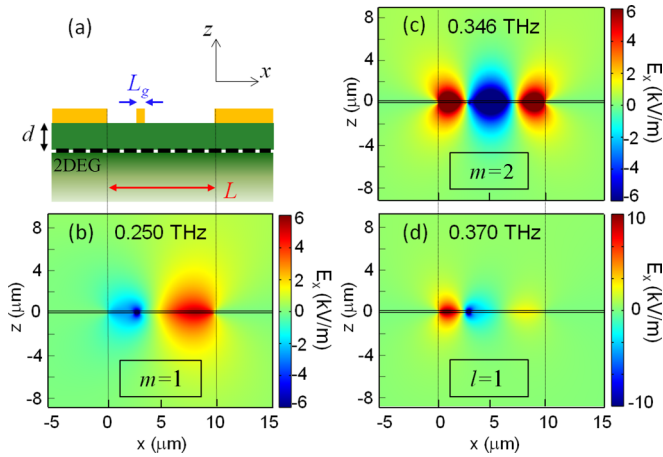
FIG. 3. (Color online) Distributions of the x component of the electric field over the cavity length ($0 < x < 10\,\mu$m) as shown in (a) the sketch of the device section, (b) calculated by FEM at the three resonant frequencies 0.250 THz, (c) 0.346 THz, and (d) 0.370 THz for $N_{2D} = 2.2 \times 10^{11}$ and $N_{2D,g} = 0.8 \times 10^{11}$ cm^{-2}. The electric-field amplitude of the input radiation was set at 210 V/m at all frequencies.

asymmetric device (with an asymmetrically positioned very short metal gate), reported in Fig. 2(b). Both the measured downconverted spectrum and the simulated absorption spectrum of the asymmetric device display three main peaks at the same frequencies, although one expects different relative peak intensities for absorption and downconversion spectra as will be explained later on.

A final assignment of all three observed peaks in the experimental spectrum to the corresponding plasmon modes and an explanation for the intensity mismatch between absorption and nonlinear efficiency can be found by looking at the electric-field profiles of different plasmon modes in Fig. 3. These were extracted from simulations at the three frequencies corresponding to the calculated absorption peaks at 0.250, 0.346, and 0.370 THz. In the simulations of Fig. 3, we have set $\mu = 3 \times 10^5$ cm^2 V^{-1} s^{-1}, $N_{2D} = 2.2 \times 10^{11}$, and $N_{2D,g} = 0.8 \times 10^{11}$ cm^{-2}. The electric-field profile at 0.250 THz [Fig. 3(b)] has a single node close to the center of the $L = 10$-μm cavity with the field intensity clearly not symmetric along the x direction due to the presence of the gate closer to the left contact. This fact explains the activation of the otherwise inactive $m = 1$ mode of the symmetric cavity [the 0.25-THz peak is absent in the symmetric cavity absorption spectrum of Fig. 2(b)]. In Fig. 3(c), the electric-field profile at 0.346 THz displays two nodes along the cavity length as expected for the $m = 2$ mode. The presence of the gate does not affect the field distribution of this mode since its position corresponds to the position of one of the nodes of the in-plane electric field. This correspondence causes a high symmetry of the electric-field distribution of this mode along the cavity length producing an almost equivalent flow of the downconverted dc current in the two opposite x directions that nearly cancel each other. This fact justifies the fairly weak downconverted signal at 0.35 THz originated from the strongly absorbing $m = 2$ plasmon mode, whereas the other two modes display a strongly asymmetric electric-field distribution, that increases the downconversion efficiency

relative to the absorption [see Fig. 2(b)]. In Fig. 3(d) the electric-field distribution of the plasmon mode at 0.370 THz is plotted. It is seen that the electric field of this plasmon mode locates in the gated region of the channel while also being extended well beyond the gated region in both x directions but much more pronounced towards the closer left contact. This indicates that the mode originated from the $l = 1$ gated mode is indeed a hybrid one, involving both gated and ungated portions of the diode channel. The much stronger dipole moment of the electron oscillations in the ungated parts of the channel makes it possible to observe this mode in the absorption spectrum.

We have seen that the cavity defect formed by the short gate in the device produces virtually no effect on the plasmon mode frequency but has a drastic positive impact on the downconversion efficiency. In order to make the defect stronger (weaker), one can then deplete (accumulate) electrons in the 2DEG region under the gate, i.e., decrease (increase) $N_{2D,g}$ by applying a gate-to-channel dc potential [22]. In Fig. 4(a), we show the measured spectra from $N_{2D,g} = N_{2D} = 2.2 \times 10^{11}$ to $N_{2D,g} < 0.5 \times 10^{11}$ cm^{-2}, whereas in Fig. 4(b) the image plot of the calculated absorption spectrum vs $N_{2D,g}$ is reported
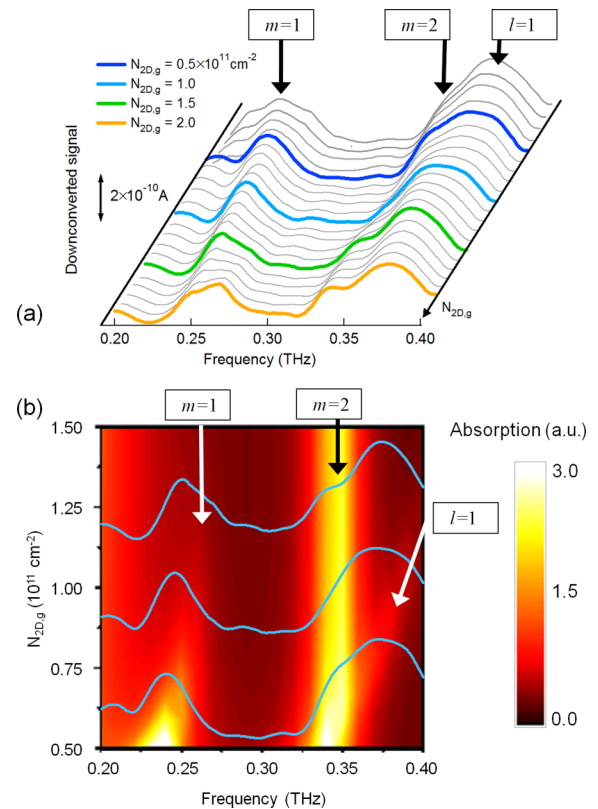

FIG. 4. (Color online) (a) Dependence of the measured downconverted signal on the electron density under the gate $N_{2D,g}$. The spectra are slightly shifted along both axes for the sake of clarity. The diagonal line with the arrow indicates the direction of increasing $N_{2D,g}$. (b) Image plot of the calculated absorption as a function of frequency and $N_{2D,g}$. The arrows indicate the peak absorption features that can be traced back to the resonant modes represented in Fig. 3. The blue lines superimposed on the plot in (b) are selected experimental spectra taken from panel (a) for $N_{2D,g} = 1.5, 0.9, 0.5 \times 10^{11}$ cm^{-2} (top to bottom).

with selected superimposed experimental spectra taken from Fig. 4(a). The frequency of the mode with $m = 2$ does not shift at all with varying $N_{2D,g}$ since its electric field is almost zero at the gate position. The $m = 1$ mode at 0.25 THz and the hybrid mode with $l = 1$ at 0.37 THz both redshift with decreasing $N_{2D,g}$ as expected, and their intensity increases relative to the $m = 2$ mode because of the higher defect strength. The frequency of pure gated plasmon resonances is expected to decrease with an approximate square-root dependence on $N_{2D,g}$ [23], but clearly the frequency of the hybrid mode does not go to zero for $N_{2D,g} \to 0$ due to the energy accumulated in the ungated portions of the cavity. For the $m = 1$ mode, the reason for the redshift is similar to that for the hybrid mode because the gated part of the channel is located in the antinode of this mode and hence effectively influences its frequency [22]. These results demonstrate that the frequency and intensity of the downconversion efficiency peaks can be tuned in our device by applying a dc gate bias. When the frequency of the hybrid mode approaches the frequency of the $m = 2$ mode for $N_{2D,g} \approx 0.5 N_{2D}$, repelled crossing due to coupling between the two modes is expected from simulations performed with negligible plasmon decay rate (see Supplemental Material S4 [21]). However, for the present electron mobility value, the plasmon decay rate is comparable with the expected value of the splitting between the interacting modes, preventing one to observe the coupling effect both in the measured and in the corresponding simulated spectra.

The peak resonant enhancement factor of the downconverted signal due to the hydrodynamic electron motion in the plasmonic microcavity was evaluated between 10 and 20 by comparing the downconverted signal from a similar device fabricated on the same wafer but not displaying resonant plasmons (see Supplemental Material S2 [21]). The absolute responsivity of the device thought as a radiation detector is 150 V/W at the peak frequency of 0.37 THz, which compares well with values of 500 V/W declared for optimized Schottky diode detectors mounted with a silicon lens [24]. These values suggest that any material system hosting 2D electrons features an intrinsic nonlinearity that can be efficiently used in the THz and infrared ranges for mixing and frequency multiplication [25–28]. Graphene devices based on the resonant ungated 2D plasma oscillation concept may be able to reach very high THz frequencies even at room temperature [29] due to the reduced population of longitudinal optical phonons that are responsible for plasmon decay if compared to our GaAs-based heterostructure [30]. Moreover, due to their dipole nature, ungated plasmon modes in an asymmetric cavity display stronger coupling to the electromagnetic field if compared to gated plasmons, that in contrast have quadrupole symmetry [31].

In conclusion, the nonlinear response of a high mobility 2DEG oscillating in the *underdamped* regime was investigated by terahertz spectroscopy in a cavity coupled to the radiation by a receiving antenna. The presence of peaks in the downconverted dc signal, corresponding to free plasma oscillation modes of the cavity, clearly points to the intrinsic nature of the nonlinearity responsible for the frequency downconversion. The asymmetry of the system required to obtain a dc signal was established by introducing a "cavity defect" formed by a short gate placed asymmetrically with respect to the center of the 2DEG channel. The presented device concept provides nonlinear efficiency enhancement due to plasmon resonances by one order of magnitude at least, and it could be transferred to other high mobility 2D electron systems, such as graphene for terahertz and infrared frequency manipulations at room temperature.

[1] M. Dyakonov and M. Shur, Appl. Phys. Lett. **87**, 111501 (2005).

[2] F. Evangelisti, J. Appl. Phys. **114**, 124506 (2013).

[3] V. V. Popov, Appl. Phys. Lett. **102**, 253504 (2013).

[4] M. Dyakonov and M. Shur, IEEE Trans. Electron Devices **43**, 380 (1996); Phys. Rev. Lett. **71**, 2465 (1993).

[5] W. Knap, Y. Deng, S. Rumyantsev and M. S. Shur, Appl. Phys. Lett. **81**, 4637 (2002).

[6] A. Shchepetov, C. Gardes, Y. Roelens, A. Cappy, S. Bollaert, S. Boubanga-Tombet, F. Teppe, D. Coiquillat, S. Nadar, N. Dyakonova, H. Videlier, W. Knap, D. Seliuta, R. Vadoklis, and G. Valusis, Appl. Phys. Lett. **92**, 242105 (2008).

[7] G. C. Dyer, S. Preu, G. R. Aizin, J. Mikalopas, A. D. Grine, J. L. Reno, J. M. Hensley, N. Q. Vinh, A. C. Gossard, M. S. Sherwin, S. J. Allen, and E. A. Shaner, Appl. Phys. Lett. **100**, 083506 (2012).

[8] V. M. Muravev and I. V. Kukushkin, Appl. Phys. Lett. **100**, 082102 (2012).

[9] G. C. Dyer, G. R. Aizin, S. J. Allen, A. D. Grine, D. Bethke, J. L. Reno, and E. A. Shaner, Nat. Photonics **7**, 925 (2013).

[10] G. C. Dyer, G. R. Aizin, S. J. Allen, A. D. Grine, D. Bethke, J. L. Reno, and E. A. Shaner, Opt. Express **22**, 16254 (2014).

[11] V. V. Popov, O. V. Polischuk, and M. S. Shur, J. Appl. Phys. **98**, 033510 (2005).

[12] L. Fetter, Ann. Phys. (N.Y.) **81**, 367 (1973).

[13] G. R. Aizin and G. C. Dyer, Phys. Rev. B **86**, 235316 (2012).

[14] E. Chow, H. P. Wei, S. M. Girvin and M. Shayegan, Phys. Rev. Lett. **77**, 1143 (1996).

[15] M. J. M. de Jong and L. W. Molenkamp, Phys. Rev. B **51**, 13389 (1995).

[16] G. C. Dyer, G. R. Aizin, S. Preu, N. Q. Vinh, S. J. Allen, J. L. Reno, and E. A. Shaner, Phys. Rev. Lett. **109**, 126803 (2012).

[17] A. Di Gaspare, R. Casini, V. Foglietti, V. Giliberti, E. Giovine, and M. Ortolani, Appl. Phys. Lett. **100**, 203504 (2012).

[18] R. Casini, A. Di Gaspare, E. Giovine, A. Notargiacomo, M. Ortolani, and V. Foglietti, Appl. Phys. Lett. **99**, 263505 (2011).

[19] V. Giliberti, A. Di Gaspare, E. Giovine, A. Lisauskas, S. Boppel, H. G. Roskos, and M. Ortolani, Appl. Phys. Lett. **103**, 093505 (2013).

[20] V. Giliberti, R. Casini, A. Di Gaspare, A. Lisauskas, H. G. Roskos, and M. Ortolani, *Infrared, Millimeter, and Terahertz Waves (IRMMW-THz) 2013, 38th International Conference on* (IEEE, Piscataway, NJ, 2013).

[21] See Supplemental Material at http://link.aps.org/supplemental/10.1103/PhysRevB.91.165313 for a description of the experimental methods including device fabrication and electro-optic setup, and for the discussion of further results mentioned in the text concerning nonresonant plasma wave devices and calculation of the anticrossing behavior.

[22] V. V. Popov, A. N. Koudymov, M. Shur, and O. V. Polischuk, J. Appl. Phys. **104**, 024508 (2008).

[23] S. J. Allen, D. C. Tsui, and R. A. Logan, Phys. Rev. Lett. **38**, 980 (1977).

[24] http://vadiodes.com/index.php/en/products/detectors.

[25] V. V. Popov, O. V. Polischuk, A. R. Davoyan, V. Ryzhii, T. Otsuji, and M. S. Shur, Phys. Rev. B **86**, 195437 (2012).

[26] E. Hendry, P. J. Hale, J. Moger, A. K. Savchenko, and S. A. Mikhailov, Phys. Rev. Lett. **105**, 097401 (2010).

[27] L. Vicarelli, M. S. Vitiello, D. Coquillat, A. Lombardo, A. C. Ferrari, W. Knap, M. Polini, V. Pellegrini, and A. Tredicucci, Nature Mater. **11**, 865 (2012).

[28] J. D. Cox and F. J. Garcia de Abajo, Nat. Commun. **5**, 5725 (2014).

[29] M. Mittendorff, S. Winnerl, J. Kamann, J. Eroms, D. Weiss, H. Schneider, and M. Helm, Appl. Phys. Lett., **103**, 021113 (2013).

[30] H. Yan, T. Low, W. Zhu, Y. Wu, M. Freitag, X. Li, F. Guinea, P. Avouris, and F. Xia, Nat. Photonics **7**, 394 (2013).

[31] V. V. Popov and O. V. Polischuk, Tech. Phys. Lett. **36**, 272 (2010).